Supplementary Information

Supplementary Methods

Mice: All experimental procedures followed the guidelines of the Harvard University and Boston Children's Hospital Institutional Animal Care and Use Committees. C57Bl/6J mice (JAX 000664), PV-GFP mice (1), GAD65-/- mice (2), Lynx1-/- mice (3) were bred in house. All genotypes used were previously backcrossed to produce congenic strains. Mice were given *ad libitum* access to food and water. Mice were maintained on a 12 hr light/dark cycle, with the exception of dark-reared animals, which were born in a dark room and first exposed to light at the start of the experiment.

Monocular Deprivation: Mice were sedated with isoflurane (2% in oxygen) and one eyelid trimmed and sutured shut as previously described (4). For deprivation lasting multiple days, the integrity of the suture was checked daily; mice in which the suture opened and the eye was exposed were discarded from the experiment.

EEG surgery and recording: Mice were anesthetized with isoflurane (2% in oxygen) and prepared for surgery using sterile technique. A small incision was made in the skull and a recording electrode (stainless steel wire, 100 μm diameter, 1 mm exposed tip) slipped between the skull and cortex (recording sites: V1 reference/ground 1 mm posterior to bregma and 2 mm bilaterally from midline, EEG 3 mm lateral of lambda; S1 reference/ground 1.5 mm anterior to bregma and 2 mm bilaterally from lambda, EEG 2 mm lateral of lambda and 1.5 mm posterior to bregma), and the post secured with dental cement. Following at least 4 days of recovery one eye was sutured shut and EEG recording begun 10 minutes following recovery from anesthesia. Recordings were performed in a sound proof box and mice housed in a cylindrical chamber containing bedding, food, hydrogel and nesting material. EEG was recorded for 5 hours with a sampling rate of 256Hz. The EEG signal was filtered through a preamplifier (Pinnacle Technology 8202-SL, high-pass filter 0.5 Hz, x100 gain), run through a humbug to reduce 60 Hz noise contamination, and further amplified (brownlee x20 gain). Data was collected using either VitalRecorder (Kissei) or Sirenia Acquisition (Pinnacle Technology). In some adult mice screws were secured to the skull in place of the wire electrodes.

EEG analysis: Initial EEG data analysis was carried out in Sleep Sign (Kissei). The EEG trace was epoched into 10 second bins, and classified by eye as wake, REM or NREM sleep, with motion artifacts discarded. Power was extracted using Short-Time Fast Fourier Transform for successive 1 minute time segments, for frequencies 1-80 Hz. Data was tapered using the Hann function. Further data analysis was carried out in Matlab (Mathworks). Unless otherwise noted, EEG power from wake epochs was used for analysis. To facilitate comparison between mice, the wake power spectrum was normalized to NREM power. The peak amplitude and frequency represent the maximum point in the power spectrum following normalization and 1/f slope subtraction.

Pharmacological administration: 20 mg/kg diazepam was administered via intraperitoneal injection once a day for three days. Control mice were administered a 1:1 mixture of saline and propylene glycol to match the diazepam solvent (5). Clopidrogel or minocycline (Sigma) were injected intraperiotoneally at 50 mg/kg in saline either 15 or 60 min prior to brief MD.

Eye injections: Mice were anesthetized with 2% isofluorane and injected with 2 μl of a 2% solution of cholera toxin β subunit conjugated with Alexa 488 (Green) or 594 (Red) (Invitrogen, Carlsbad, CA) using a Hamilton® syringe. After 2 days, mice were deeply anesthetized and sliced according to the visual TC protocol. Slices were placed in 4% paraformaldehyde overnight, cryoprotected in 30% sucrose and sub-sectioned to 50 μm on a freezing Vibratome (Leica), maintaining the initial plane.

Slice Preparation: Mice were anesthetized with isoflurane then rapidly decapitated. The brain was removed and placed in an ice-cold choline-based cutting solution (in mM: 78.3 NaCl, 23 NaHCO3, 23 glucose, 33.8 choline chloride, 2.3 KCl, 1.1 NaH2PO3, 6.4 MgCl2, and 0.45 CaCl2) (6). 500 μm thick visual TC slices were sectioned on a vibratome (Microm HM 650V, Thermo Scientific) using a sapphire blade. The visual TC slice was previously described by MacLean et al. (7). Briefly the brain was mounted on a 55 ° agar mold and one 500 μm thick slice was sectioned 300 μm after the disjoining of the corpus callosum. Slices were incubated at 35 °C in oxygenated ACSF (125 mM NaCl, 25 mM glucose, 25 mM NaHCO3, 2.5 mM KCl, 2 mM CaCl2, 1.25 mM NaH2PO4 and 1 mM MgCl2 (310 - 320 mOsm) for at least 15 min, before returning to $20 - 22$ °C.

Voltage Sensitive Dye Imaging (VSDI): VSDI and analysis were performed as previously described (8). Slices were incubated for at least 90 min in the the voltage-sensitive dye Di-4-ANEPPS (Invitrogen; 5 μg/ml in ACSF) before transfer to an ACSF $(20 - 22$ °C) recording chamber. Slices were imaged using an Olympus MVX10 microscope with 4x objective. Excitation light from a shuttered 150 W halogen lamp was band-pass filtered (515 and 535 nm) and reflected toward the sample by a 570-nm dichroic mirror. Emitted fluorescence was long-pass filtered (590 nm) and imaged using a MiCam Ultima CMOS-based camera (SciMedia). A 1 ms stimulating pulse was delivered to the LGN using a bipolar glass stimulating electrode filled with ACSF. Fluorescent changes for a single stimulation trial were collected at 1 ms frame rate for 512 ms and averaged across ten sweeps. Regions of interest containing 5 x 5 pixels covering 125 x 125 μm were spatially integrated using MiCam Ultima analysis software. Individual time course traces were subsequently exported to Igor Pro (WaveMetrics) for custom analysis (8). Fluorescence change was normalized to resting fluorescence (ΔF/F0). Response amplitude was defined as maximum fluorescence change (ΔF/F) per trial at a given region of interest. Variations in daily preparation were normalized by slice; all signals were divided by the change in fluorescence measured in the upper region at a stimulating strength of 0.1 mA.

Acute Slice Electrophysiology: Prior to recording, slices equilibrated for at least 1 hr in oxygenated ACSF before being transferred to a submersion chamber for room temperature recording. Layer 4 non PV or PV cells were targeted by shape and GFP expression using a combination of infrared-Nomarski DIC optics and fluorescent microscopy (Eclipse FNI, 40X immersion objective, Nikon). Recordings were obtained on an Axon MultiClamp 700B amplifier and digitized at 10 kHz (Axon Digidata 1440A). Recording electrodes (2-4MΩ) were fabricated from borosilicate glass microcapillaries (outer diameter, 1.5 mm) with a micropipette puller (DMZ Universal Puller). For whole-cell voltage-clamp recordings the internal solution contained (in mM) 120 Cs-methanesulfonate, 6 CsCl, 2 MgCl2, 0.05 CaCl2, 20 HEPES, 0.02 EGTA, 10 phosphocreatine di(Na) salt, 4 Mg-ATP, 0.4 Na3-GTP, 0.15% biocytin, and 1 lidocaine derivative QX-314 (pH 7.2 with CsOH, 290 - 300 mOsm). Access resistances were maintained at less than 25 MΩ throughout the experiments. TC excitatory post-synaptic currents (EPSCs) were recorded in the presence of 10μM bicuculline. and were stimulated by a bipolar glass stimulating electrode filled with ACSF placed in the LGN or the fiber bundle exiting the LGN. Incremental stimulus intensities were delivered at 0.05 Hz until an evoked EPSC was discernible from failures (6) and a consistent connection was present at a holding potential of -70 mV. TC inputs were differentiated from di-synaptic intracortical inputs on a basis of onset delay ($<$ 9 ms), low jitter and by differences in short term plasticity (9; 10).

Analysis of EPSCs and intrinsic properties was performed using pClamp10 (Molecular Devices). To record AMPA mediated mini EPSCs (mEPSCs), slices were first incubated in ACSF containing 1 μM TTX for 60 minutes prior to recordings and performed in the presence of TTX (1 μM), APV (50 μM) and bicuculline (20 μM). AMPA mEPSCs were recorded for 10 min, high pass filtered at 2 kHz and analyzed using MiniAnalysis (Synaptosoft).

Fos-GFP Single Eye Exposure: MD was performed on the left eye of four Fos-GFP+ mice (c/o Dr. Alison Barth, Carnegie Mellon U) at P22. The mice were then placed in a dark sound chamber to decrease background Fos expression by decreasing light and sound exposure. After three days the mice were exposed to a slow strobe light for 90 min. Mice were perfused transcardially with 0.9% saline followed by 4% paraformaldehyde (PFA). Brains were post-fixed in PFA for 1.5 hours. After fixation the brains were blocked on the TC angle and thinly sliced (50 μm). GFP signal was enhanced with rabbit anti:GFP antibody 1:2000 (Abcam). After determining the boundaries for the various regions, we used ImageJ "particle analysis" function with 0.5-10 μm^2 as the initial parameters to measure the density of Fos labeled cells within each region.

Puncta Immunofluorescence: Mice were perfused transcardially with paraformaldehyde (4% PFA) and the brains removed, postfixed in PFA for 1.5 hours, and cryoprotected in a 30% sucrose solution. Coronal sections (40 μm) were cut on a cryostat or freezing microtome (Leica). Every fourth section was collected and washed in phosphate buffered saline (PBS) for 30 minutes followed by 4 °C overnight incubation in blocking solution (0.8% Triton X- 100

and 20% bovine serum albumin (BSA) in 0.1 M PBS- Triton). Slices were then transferred to a primary antibody solution in 0.2% Triton X-100 and 5% BSA in 0.1 M PBS-Triton for overnight incubation. Antibodies were used at the following concentrations, rabbit anti-GFP 1:2000 (Abcam), rabbit anti-PV 1:1000 (Swant), guinea pig anti-VGluT2 1:500 (Synaptic Systems). After 3 x 15 min washes in PBS-Triton-BSA, sections were incubated overnight in secondary antibody, goat anti-rabbit IgG Alexa 488, goat anti-rabbit IgG Alexa 596, goat anti-guinea pig 564, goat anti mouse 488 or 633 (Invitrogen), diluted at 1:1000 in PBS-Triton-BSA. Sections were washed three times in PBS-Triton for 30 min prior to being mounted on glass slides. The number of VGluT2 immunoreactive puncta surrounding a PV+ cell body were estimated using a custom MatLab script. PV+ positive cells were imaged on a Fluoview FV1000TM scanning microscope (Olympus®) at 100x. Automatic thresholding within MatLab defined the region of the PV+ cell. This region was then used to select a 1.25 μm ring around the neuron. The red VGluT2 channel was thresholded to the median intensity plus 4x the standard deviation and all puncta within the ring, larger than 3 pixels (0.123 μm), were automatically counted and analyzed (Supp Fig. 11).

Statistical Analysis: Population data were expressed as the mean $\pm$ SEM. Data were initially analyzed with the Kolmogorov-Smirnov test for normality to guide subsequent analysis. Normally distributed data was analyzed using Student's t test (for two groups) or ANOVA with Tukey's Comparison Test; all other data was analyzed using the Mann-Whitney test (for two groups) or Kruskal-Wallis test with Dunn's Multiple Comparison test. Analysis was done using Prism software (Graphpad, San Diego, CA).

Computational Model

Neurons

The objective of our mathematical models is to suggest possible network activity involved in the generation of MD-induced γ-oscillations and explore the relationship between the emergent γ and decreased thalamocortical AMPA conductance. We construct a thalamocortical network using single-compartment, conductance-based models of layer IV cortical pyramidal cells (PYR), layer IV cortical PV+ interneurons (PV) and thalamocortical cells (TC cells). Neuronal voltages (V) change with time according to a differential equation that equates the capacitive membrane current with the channel currents:

$$c_m \frac{dV}{dt} = -\sum I_{memb} - \sum I_{syn} + I_{app} \tag{1}$$

Membrane voltage (V) is measured in mV. Currents have units in $\mu A/cm^2$. The specific membrane capacitance (c_m) is held at $1\mu F/cm^2$ for all simulations. The individual collection of membrane and synaptic current, I_{memb} and I_{syn},

respectively, as well as the background excitation term (I_{app}) determine the dynamics of each type of neuron. All neurons contain spiking membrane currents consisting of a fast sodium current (I_{Na}), a fast potassium current (I_K) and a leak current (I_L). The PYR cells also have an M-current (I_M) to account for the spike-frequency adaptation observed in this cell type. We modeled our TC cells during awake, relay states. Thus, the TC cells included only the spiking membrane currents and did not include any low-threshold membrane currents, which are known to play a role in oscillatory activity during sleep and anesthetic states.

All membrane have Hodgkin-Huxley-type conductances formulated as:

$$I = \bar{g} m^n h^k (V - E_{ion}) \tag{2}$$

The maximal conductance of the membrane currents $(\bar{g})$ is held constant, The reversal potential for each current (E_{ion}) is constant and has units of mV. The activation gating variables (m) and inactivation gating variable (h) are unit-less variables between 0 and 1. The number of gating variables is n for the activation gate and k for the inactivation gate. The activation and inactivation gating variables evolve in time according to a two-state kinetic equation formulated (written for the gating variable m) as:

$$\frac{dm}{dt} = \frac{m_\infty - m}{\tau_m} \tag{3}$$

The steady-state function (m_∞) and the time constant of decay (τ_m) can be re-written as rate functions for each current (α_m, β_m) by using the equations:

$$m_\infty = \alpha_m / (\alpha_m + \beta_m)$$
$$\tau_m = 1/(\alpha_m + \beta_m).$$

Models of the spiking currents (I_{Na}, I_K, I_L) for the PYR, PV and TC cells are from (11).

Fast sodium current: The rate functions for the sodium current activation (m) and inactivation (h) variables are formulated as:

$$\alpha_m = \frac{0.32(V + 54)}{1 - \exp\left[-(V + 54)/4\right]}$$
$$\beta_m = \frac{0.28(V + 27)}{\exp\left[(V + 27)/5\right] - 1}$$
$$\alpha_h = 0.128 \exp\left[-(V + 50)/18\right]$$
$$\beta_h = \frac{4}{1 + \exp\left[-(V + 27)/5\right]}$$

The maximal conductance of the sodium current is $\bar{g}_{Na} = 100mS/cm^2$. The sodium reversal potential is $E_{Na} = 50mV$. The sodium current has three activation gates $(n = 3)$ and only one inactivation gate $(k = 1)$.

Fast potassium current: The fast potassium current (I_K) has four activation gates $(n = 4)$ and no inactivation gates $(k = 0)$. The rate functions of the activation gate are described by:

$$\alpha_m = \frac{0.032(V + 52)}{1 - \exp\left[-(V + 52)/5\right]}$$

$$\beta_m = 0.5\exp\left[-(V + 57)/40\right]$$

The maximal fast potassium channel conductance is $\bar{g}_K = 80mS/cm^2$. The reversal potential for potassium is $E_K = -100mV$.

Leak Current: The leak current (I_L) has no gating variables $(n = 0, k = 0)$. The maximal conductance of the leak channel is $g_L = 0.1mS/cm^2$. The leak channel reversal potential is $E_L = -67mV$.

M-current: The model of the M-current comes from (12). The M-current has one activation gate $(n = 1)$ and no inactivation gate $(k = 0)$. The rate functions for the M-current activation gate are described by:

$$\alpha_m = \frac{Q_s 10^{-4}(V + 30)}{1 - \exp\left[-(V + 30)/9\right]}$$

$$\beta_m = -\frac{Q_s 10^{-4}(V + 30)}{1 - \exp\left[(V + 30)/9\right]}$$

We use a Q_{10} factor of 2.3 to scale the rate functions of the M-current since the original formulation of these kinetics described dynamics at $23\,^\circ\mathrm{C}$ (12). Thus, for a normal body temperature of $37\,^\circ\mathrm{C}$, the M-current rate equations are scaled by Q_s, which is formulated as:

$$Q_s = Q_{10}^{(37\,^\circ\mathrm{C} - 23\,^\circ\mathrm{C})/10} = 3.209$$

The maximal M-current conductance is $\bar{g}_m = 1.29mS/cm^2$ for the normal striatum.

Synaptic Connections

Our models contains two types of synaptic currents: AMPA currents (I_{AMPA}) and GABAa currents (I_{GABAa}). Both synaptic currents (I_{syn}) derived from (11) and used Hodgkin-Huxley dynamics formulated as:

$$I_{syn} = \bar{g}s(v_{pre})(V - E_{ion}) \tag{4}$$

Each synaptic current has a single activation gate (s) that depends on the voltage of the pre-synaptic neuron (v_{pre}). E_{ion} is the synaptic reversal potential, and g is the maximal synaptic conductance.

The inhibitory GABAa current is modeled as:

$$I_{GABAa} = \bar{g}_i s_i (V - E_i)$$

The gating variable for inhibitory GABAa synaptic transmission is represented by s_i. For the jth neuron in the network:

$$s_j = \sum_{k=1}^{N} S_{i_k i_j}$$

The variable $S_{i_k i_j}$ describes the kinetics of the gating variable from the kth interneuron to the jth neuron. This variable evolves in time according to:

$$\frac{dS_{i_k i_j}}{dt} = g_{GABAa}(V_k)(1 - S_{i_k i_j}) - \frac{S_{i_k i_j}}{\tau_i}$$

The GABAa time constant of decay (τ_i) is set to 10 ms. The GABAa current reversal potential (E_i) is set to -80 mV in all neurons. The rate functions for the open state of the GABAa receptor ($g_{GABAa}(V_k)$) is described by:

$$g_{GABAa}(V_k) = 2(1 + tanh(\frac{V_k}{4}))$$

The maximal GABAa conductance ($\bar{g}_i$) is 0.03 mS/cm^2 between PV cells within the same population (PVo or PV$_{MD}$) during the critical period and is 0.003 mS/cm^2 in the pre-critical period. The maximal GABAa conductance ($\bar{g}_i$) is 0.25 mS/cm^2 between PV cells of different populations during the critical period and is 0.025 mS/cm^2 in the pre-critical period. The maximal GABAa conductance between PV cells is scaled according to the number of synaptic connections received by a given cell by dividing $\bar{g}_i$ by the number of GABAa synapses made onto that cell. The maximal GABAa conductance ($\bar{g}_i$) from PV cells to PYR cells changes according to plasticity rules (see section entitled "Plasticity Rules").

The activation gate of AMPA current is described mathematically by the equation:

$$I_{AMPA} = \bar{g}_e s_e (V - E_e)$$

The variable s_e represents the sum of the synaptic activation variables from all excitatory cells projecting to the neuron receiving the AMPA input. For the jth neuron:

$$s_e = \frac{1}{N} \sum_{k=1}^{N} S_{e_k i_j}$$

In this formula, N is the number of excitatory cells that make connections with the jth neuron. The kinetics of the synaptic activation variable from excitatory cell k to neuron j are denoted by $S_{e_k i_j}$ and described by:

$$\frac{dS_{e_k i_j}}{dt} = g_{ee}(V_k)(1 - S_{e_k i_j}) - \frac{S_{e_k i_j}}{\tau_e}$$

The time-constant of decay for the AMPA synapse is $\tau_e = 6ms$ for TC cell synapses onto PYR cells and $\tau_e = 2ms$ for TC cell synapases onto PV cells. The rate function for the open state, $g_{ee}(V_k)$, which is dependent on the membrane voltage of the kth pre-synaptic excitatory cell follows the mathematical formulation:

$$g_{ee}(V_k) = 5(1 + tanh(\frac{V_k}{4}))$$

The maximal AMPA conductance ($\bar{g}_e$) changes with plasticity rules (see "Plasticity Rules" section). The maximal AMPA conductance is scaled according to the number of AMPA synaptic connections received by a given cell by dividing g_e by the number of AMPA synapses made onto that cell. The reversal potential for all AMPA synapses is $E_e = 0mV$.

Gap junction connections were present between all PV cells of the same population (PVo or PV_{MD}) during the critical period. These connections were absent during the pre-critical period. The gap junctional current from neuron j to neuron i was modeled as:

$$I_{gap} = \bar{g}_{gap}(V_i - V_j)$$

The maximal gap junction conductance was $\bar{g}_{gap} = 0.01$ mS/cm^2 during the critical period unless otherwise stated.

Networks and LFP

Our networks consist of 40 cells of each type: TC cells, PYR cells and PV cells. All intracortical connections are very weak (silent synapses) initially. In the pre-CP, each PV cell connects weakly to all PYR cells (gGABAa = 0.01 mS/cm^2). These synapses evolved in strength according to the plasticity rules. We originally included weak PYR to PV cell connections. However, since the PYR to PV plasticity rule is bilaterally depressing (13), these synapses remained weak and did not appreciably affect network dynamics. Thus, for the simulations presented in this work, we did not include PYR to PV synapses. Additionally, we did not include excitatory connections between PYR cells. We constructed two populations of PV cells: one receiving TC input relayed from the right

eye and the other receiving TC input originating from the left eye (Fig. 6A). Although it is unknown whether PV cells in layer IV of V1 are monocular or binocular, we assumed monocular input based on the literature surrounding ocular dominance columns, which are defined by their selective, monocular input to layer IV. Though ocular dominance columns are not found in mice, we made the assumption that the underlying networks in the binocular zone of mouse V1 resemble ocular dominance columns. Thus, although the neurons in these networks overlap in space, unlike the clear ocular dominance columns present in other mammals, we assumed that the same network principles apply, including monocular input to PV neurons of layer IV of V1. PV cells are connected all-to-all and weakly in the pre-CP. We assume there is greater competition between PV populations than within populations, and thus GABAa conductance is stronger for inhibitory connections between versus within populations (see SI "Synaptic Connections" section for conductance values).

The two TC populations connect to all PV cells in their respective population of PV cells. Thus, each PV cell receives 20 TC inputs. Pyramidal cells receive TC input from all TC cells relayed from both eyes. Initially in the pre-CP, each TC cell connects relatively strongly to one pyramidal cell (gAMPA = $0.12\ mS/cm^2$) and one PV cell (gAMPA = $0.25\ mS/cm^2$), and conversely, each PV and PYR cell receives only one strong TC connection. All other TC connections to PYR and PV cells are very weak (silent) (gAMPA = $0.001\ mS/cm^2$ for weak TC-to-PV synapses and gAMPA = $0.0001\ mS/cm^2$ for weak TC-to-PYR synapses) (Fig. 6A). We constructed our model with only one strong TC connection to each PV and PYR cell in order to account for the strong topographic organization that is present in the early thalamocortical system (22; 23; 24), the initially sparse innervation of cortex by thalamus (25), as well as the abundance of silent synapses in early networks (26). After initialization, the TC-to-cortex connections evolve according to plasticity rules (see SI section "Synaptic Plasticity Rules").

The CP state is modeled by adding electrical connections between PV cells and strengthening PV-to-PV inhibition (see SI "Synaptic Connections" section for conductance values). At CP onset, PV cells connect electrically with all other PV cells of their own population (those receiving input derived from the right or left eye, respectively), and GABAa connections between all PV cells are strengthened by a factor of 10, since the critical period is accompanied by strengthened inhibition (17).

We model monocular deprivation (MD) by stopping the spiking of half of the TC cells (those receiving input from the deprived eye), which effectively stops the spiking of all PV and pyramidal cells to which those TC cells project strongly. We refer to the population of PV cells deprived of TC input as PV_{MD} cells and to the population of PV cells receiving TC input from the open eye as PVo cells (Fig. 6A).

We model the local field potential (LFP) as the sum of inhibitory currents onto pyramidal cells (19; 20; 21). Spectrograms of the model LFP were obtained

using the multitaper power spectral density estimate in MatLab.

We model homeostatic changes due to sleep by decreasing gap junction conductance between PV cells. The maximal PV-to-PV gap junction conductance is lowered from $0.01mS/cm^2$ to $0.0085\ mS/cm^2$ after the first period of sleep and to $0.001\ mS/cm^2$ after the second period of sleep. Sleep is not simulated physiologically since our intent for putting in bouts of "sleep" is solely to demarcate the boundary between two different levels of PV gap junctional conductance as seen in Fig. 7A. As such, "sleep" periods are put in our model by hand by reducing cortical PV spiking by decreasing the maximal sodium conductance of the PV cells to $10\ mS/cm^2$. This effectively removes all high frequency activity from the simulated LFP.

Background excitation

Only TC cells had a background excitation current: $I_{app} = 0.2\ \text{mS/cm}^2$. The TC cells also had Gaussian random noise input with an amplitude of $50 \times \sqrt{0.05}$, where 0.05 was the timestep of integration.

Synaptic Plasticity Rules

All AMPA synapses evolve in strength according to a Hebbian spike-time dependent plasticity (STDP) rule (18). The computational formulation of the Hebbian plasticity rule is derived from (14). In particular, we calculate the fractional change in the maximal AMPA conductance ($\omega_{i,j}$) from pre-synaptic cell i to post-synaptic cell j as:

$$\omega_{i,j} = \left\{ \begin{array}{ll} A_+ e^{-\Delta t/\tau_+} & \text{if } \Delta t \geq 0 \\ -A_- e^{\Delta t/\tau_-} & \text{if } \Delta t < 0 \end{array} \right. \tag{5}$$

In this equation, Δt is the time of spiking of the post-synaptic cell (t_j) minus time of spiking of the pre-synaptic cell (t_i): $\Delta t = t_j - t_i$. The most recent pre- and post-synaptic spikes are used in this calculation at any given time during the simulation (see "Relaxation of model assumptions" for an alternative method of counting spikes towards plasticity). The amplitude of the fractional synaptic change for potentiation is $A_+ = 0.005$, and the time constant of decay of potentiation is $\tau_+ = 14$ ms. For depression, the amplitude is $A_- = 0.0025$, and the time constant of decay is $\tau_- = 90$ ms (Supp Fig. 5F). We note that the time constant of decay of depression is longer than that used in (14) but still within the range of LTD delays suggested by experiments (15; 16). We model the effect of STDP on the maximal AMPA conductance from cell i to cell j by calculating $\bar{g}_{e_{new}} = \bar{g}_e + \bar{g}_e \cdot \omega_{i,j}$, where $\bar{g}_e$ is the value of the maximal conductance before STDP and $\bar{g}_{e_{new}}$ is the value of the maximal conductance after STDP. The STDP rule is applied after all pre-synaptic spikes and after all post-synaptic spikes.

The PV-to-PYR GABAa synapses evolve in time according to a STDP rule that favors the development of lateral inhibition. The fractional change in the

maximal GABAa conductance from pre-synaptic cell i to post-synaptic cell j follows equation (5). The amplitude of the fractional change for the GABAa when $\Delta t \geq 0$ is $A_+ = -0.005$, and the time constant of decay is $\tau_+ = 14$ ms. When $\Delta t < 0$, the amplitude of the fractional change is $A_- = 0.0025$, and the time constant of decay is 34 ms (Supp Fig. 5F).

Computational Tools

Our network models were programmed in C++. The code can be found at: `https://github.com/mmccart/Quast-et-al-C--code`

The differential equations were integrated using a fourth-order Runge-Kutta algorithm. Model output was graphed and analyzed using MatLab. We used the mulittaper method in MatLab to calculate spectral power.

Relaxation of model assumptions

Assumption of GABAa stronger between PV populations than within populations

We assumed GABAa between PV populations is stronger than within PV populations in order to model more competition between than within PV populations. If we relax the assumption of PV inhibition stronger between populations than within populations by decreasing the level of GABAa between populations to the same level as found within populations, we still see the emergence of a 40 Hz γ-oscillation, a rise in the frequency of the γ-rhythm and an eventual fade-out of the γ-oscillation (Supp Fig. 8A). However, in contrast to our original model, a γ-rhythm due to ING dynamics emerges immediately upon entering the CP (Supp Fig. 8A,B) rather emerging only after MD (compare with Fig. 6C), which is inconsistent with the experimental findings in which γ does not emerge during the CP without MD (Fig. 1B,C). This occurs due to the increased excitability of all PV cells after the addition of electrical connections, along with the inability of weak connections between PV populations to suppress the ING in either population. Additionally, different from our original model, after MD the PV_{MD} cells also produce ING, though at a slower γ-frequency than the PVo cells (Supp Fig. 8C,D). As a result of the PV_{MD} ING, a 30 Hz γ-frequency band emerges in the spectrogram along with the 40 Hz band (Supp Fig. 8A). In contrast to the 40 Hz γ-band, the 30 Hz γ-oscillation only emerges after MD (not after CP changes only), it does not increase in frequency as time progresses, and is due to 30 Hz ING in the PV_{MD} population (Supp Fig. 8A-D). The 30 Hz PV_{MD} ING occurs because the weak GABA from PVo to PV_{MD} is insufficient to suppress the additional excitability of the PV_{MD} population due to the presence of electrical connections. The 30 Hz rhythm does not change in frequency over time because no TC-to-PV_{MD} spike-time dependent plasticity can occur in the absence of spiking in the TC cell population that projects to PV_{MD} cells.

In contrast, if we relax our original assumption about connectivity strengths between PV cells by increasing the maximal conductance of GABAa between

PV cells within a population to the same level of GABAa between populations, we no longer see the rise in gamma power (Supp Fig. 8E) or the formation of a clear ING rhythm among the PVo cells (Supp Fig. 8F-H). On the network level, we occasionally see some bouts of synchronous activity among PV cells after MD (Supp Fig. 8G) but these are infrequent and can occur in both PVo and PV_{MD} cell populations. The occasional spiking of PV_{MD} cells after MD occurs due to more inhibition among PVo cells slowing them down such that they provide less inhibition to PV_{MD} cells. Since all PV cells have electrical connections in the CP, which elevates their excitation, PV_{MD} occasionally have enough excitability to spike even in the absence of TC input. However, even with simulations lasting as long as 500 s of simulation time, there is no evidence of ING formation (Supp Fig. 8H). The lack of ING is the result of the increased inhibition between PV cells of the same population, which decreases the excitation of the PV cells not allowing ING to readily form.

Assumption of one-to-one strong TC-to-PV synpases

When one TC-to-PV connection is significantly stronger than the others in the pre-CP, no plasticity occurs in the pre-CP (Supp Fig. 9A,B), no gamma emerges in the pre-CP (Fig. 9C) and network dynamics do not change over the course of the CP (compare Supp Fig. 9D (late pre-CP) and Fig. 6B (early pre-CP)). We relaxed this assumption of strong 1:1 TC-to-PV connectivity in our initial (pre-CP) network by allowing three TC cells to project strongly, with approximately the same strength, to each PV cell in the network, while keeping the rest of the TC-to-PV connections weak. We find that this initial network state allows the TC-to-PV synapses to transition to a more homogeneous state in the pre-CP (Supp Fig 9E,F). Although ING does not emerge due to lack of gap junctions in the pre-CP, broadband power in the model LFP becomes apparent after the TC-to-PV plasticity has taken place (Supp Fig. 9G). As in our CP+MD networks, the evolution of the TC-to-PV synapses to homogeneity results in more excitation to the PV cells, as well as the PV cells responding to the TC population input rather than individual TC cell input (Supp Fig. 9H).

This pre-CP transition occurs because the ongoing competition between the strong synapses continually leaves one of the stronger synapses temporarily weakened, allowing the silent synapses the opportunity to strengthen. Since there is a upper limit to the total amount of excitation a neuron can receive, strengthening silent synapses prevents the weakened strong synapses from strengthening even if the pre-post timing is conducive to LTP. In comparison, when one synapses is significantly stronger than the others, the strong synapses always drives its PV neuron to spike with the pre-post timing that keeps this synapses strong, not allowing the opportunity for other synapses to strengthen. Thus, these results suggest that in order to observe the MD-induced gamma rhythm only during the CP, as seen experimentally, the underlying thalamocortical structure must initially consist of one TC-to-PV connection significantly stronger than the others. Our models suggest this is a necessary condition

that allows stable pre-CP dynamics and prevents thalamocortical networks from rewiring TC-to-PV connections to a more homogeneous state before the CP.

Alternative method of spike counting for synaptic plasticity rule

The plasticity rules take into account the most recent pre- and post-synaptic spikes to determine the fractional change in the maximal synaptic conductance. This method works well when pre- and post-synaptic spiking rates are similar. However, if pre- and post-synaptic spiking rates are significantly different, then this method may bias the plasticity towards either LTP or LTD. In our simulations during CP with MD, the PVo cells spike faster than the TCo cells, which could bias the TC-to-PV plasticity towards LTP. Thus, we ran simulations using an unbiased method of counting spikes towards plasticity for the AMPA synapses from TC to PVo. Specifically, this method uses only the PV cell spike immediately before and immediately after each TC cells spike to determine plasticity. With this rule, the number of spikes that contribute to LTP and LTD at the TC-to-PVo synapses are equivalent. With this unbiased method of counting spikes, our results remain qualitatively the same: we observed an abrupt onset of γ with MD that increases in frequency and eventually fades out (Supp Fig. 10A), the strong TC-to-PVo synapses decrease in strength while the initially silent TC-to-PVo synapses increase in strength (Supp Fig. 10B), random spiking in the pre-CP (Supp Fig. 10C) is replaced by ING in the PVo population during the early CP MD state (Supp Fig. 10D). The only difference observed was a longer time for the γ-oscillation to rise in frequency and fade out (compare Supp Fig. 10A using the unbiased counting method and Fig. 6C using the original plasticity counting method).

Supplementary Figures
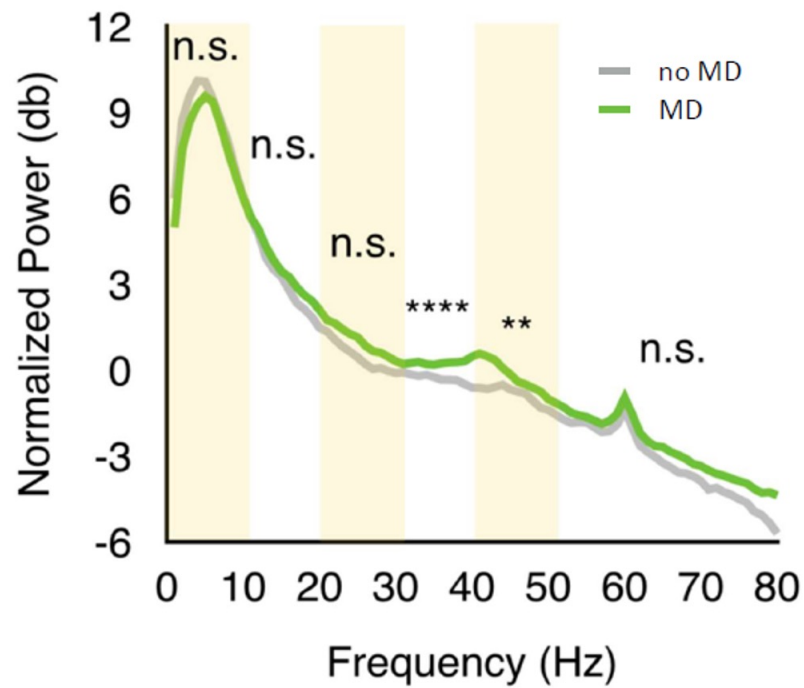
Supp Fig 1: **Monocular deprivation triggers a selective increase in γ power over the visual cortex.** Mean power during the first hour of wake comparing no MD and MD conditions in juvenile mice. Power between the two groups was compared using a Mann Whitney test over the following frequency ranges (in Hz): 1-10, 11-20, 21-30, 31-40, 41-50, 51-80. The only significant differences in power fell in the low gamma range (31-50 Hz). **** $P < 0.0001$, ** $P < 0.01$.
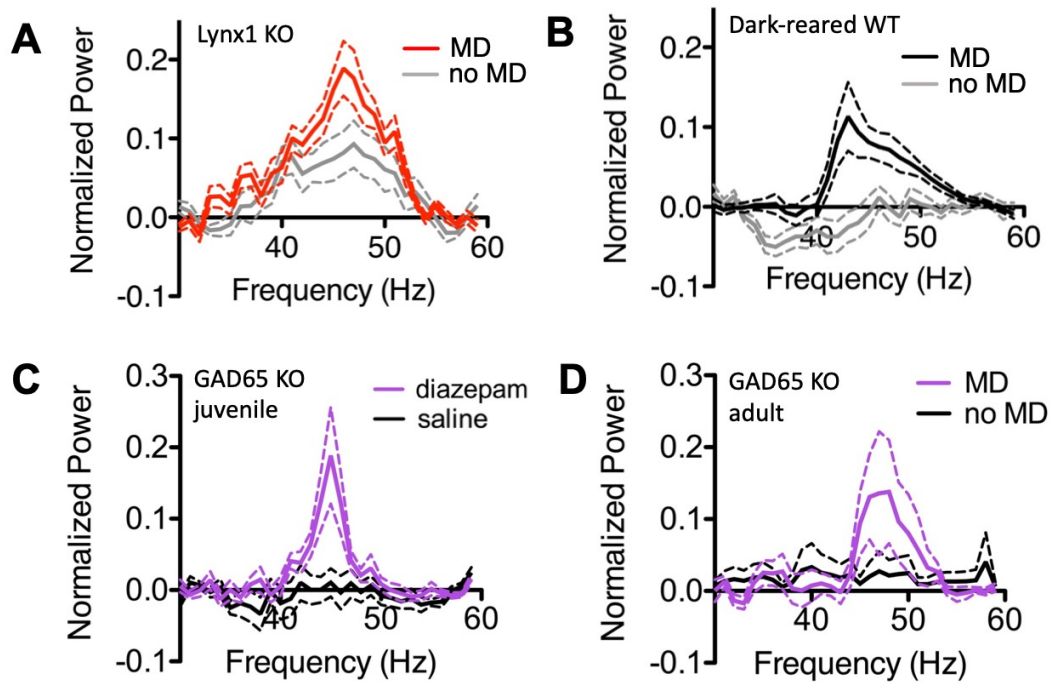
Supp Fig 2: γ **power rise in models of altered CP plasticity.** (A) Mean EEG power of adult Lynx1 KO mice with (red) or without (gray) MD in the γ frequency range for the first hour following MD. (B) Mean EEG power of adult dark reared mice with (black) or without (gray) MD in the γ frequency range for the first hour following MD. (C) Mean EEG power in the γ frequency range for the first hour following MD in Gad65 KO juvenile mice treated with diazepam (light purple) or saline (gray) and Gad65 KO adult mice treated with diazepam (dark purple). Gad65 KO mice treated with diazepam but without MD did not show an increase in γ power (black). EEG power is normalized to NREM γ power, dashed lines show SEM.
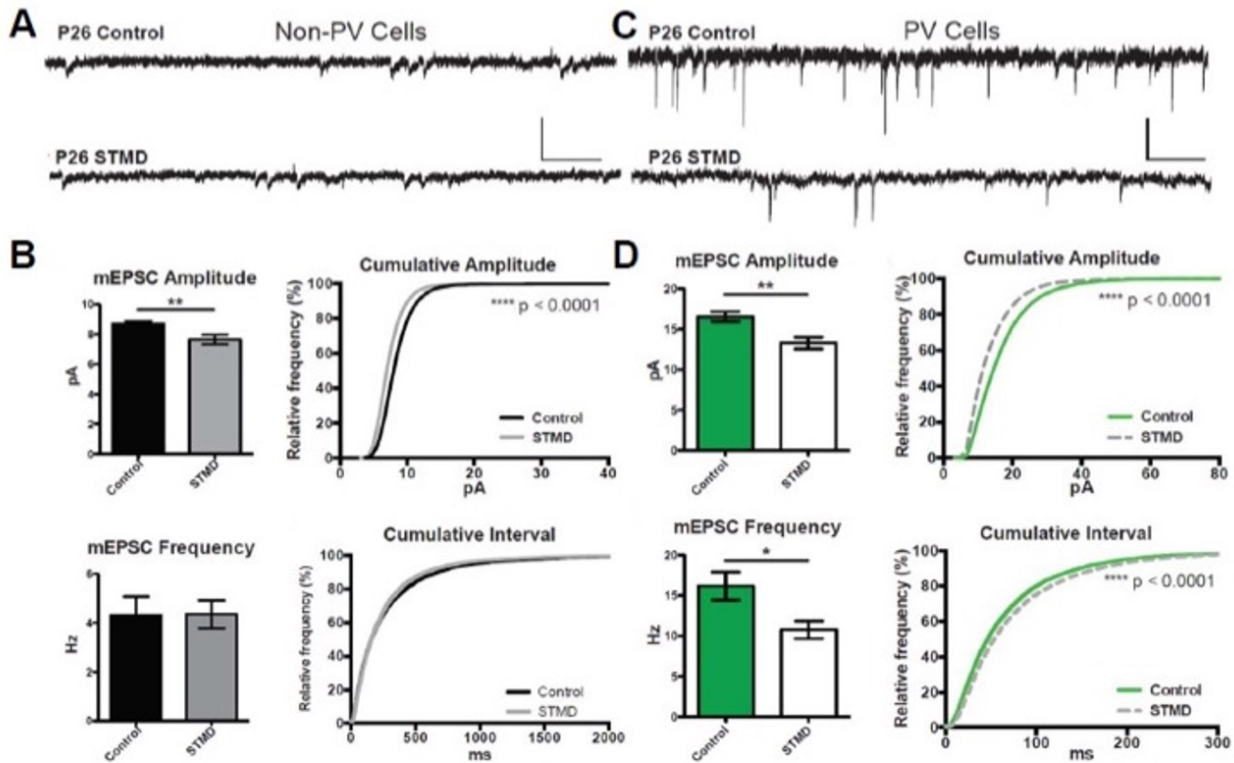
Supp Fig 3: **Thalamocortical synapse strength is reduced following STMD.** (A) Sample mEPSC traces from control P26 mouse (top), and P26 STMD mouse (bottom) from both non-PV and PV cells. Scale bars: 100 ms, 20 pA. (B) There is a small but significant decrease in mean mEPSC amplitude (Student's t test) and (C) right shift in cumulative amplitude in non-PV cells (500-1000 events per cell, Mann-Whitney test; Control n=7, MD n=8). (D) Quantification of significant decrease in mean mEPSC amplitude (Student's t test) and (E) right shift in cumulative amplitude in PV+ cells (1000-1500 events per cell, Mann-Whitney test; Control n=7, MD n=9). There is no significant difference in the mean frequency (F) or cumulative interval (G) for the non-PV cells but a significant decrease in the PV cells (H and I). Bar graph values are mean $\pm$ SEM. *P<0.05, **P<0.01,****P<0.0001.
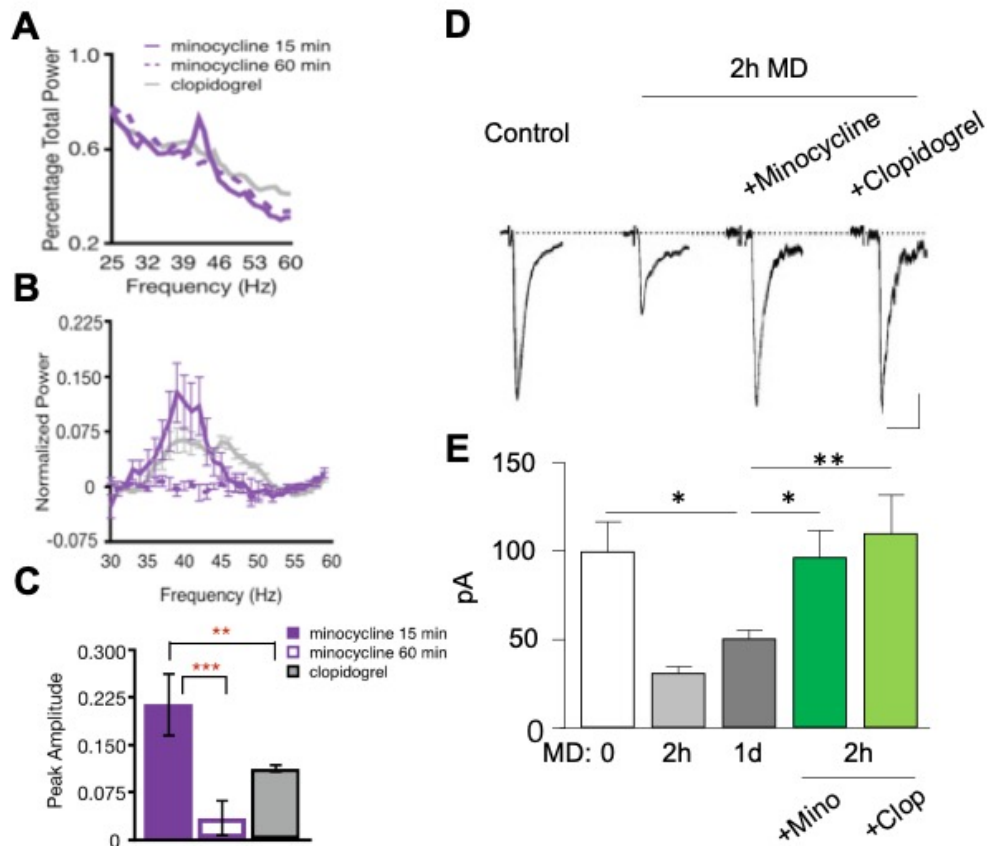
Supp Fig 4: **Microglial inhibitors prevent both rapid g-rhythm induction and TC-to-PV synapse weakening.** (A) Mice received intraperitoneal (i.p.) injections (50mg/kg) of either minocycline or clopidogrel before monocular deprivation (MD). Gamma power peak was curtailed in a time dose-dependent manner, being blocked 1 hour (hollow purple or grey bars, respectively) but not 15 min (solid purple) after treatment. (B) Similarly, both drugs administered 1 hour prior to MD for 2 hours, prevented the loss of thalamocortical input onto PV-cells. N=6 mice each, *P<0.05; **p<0.01; ***p<0.005
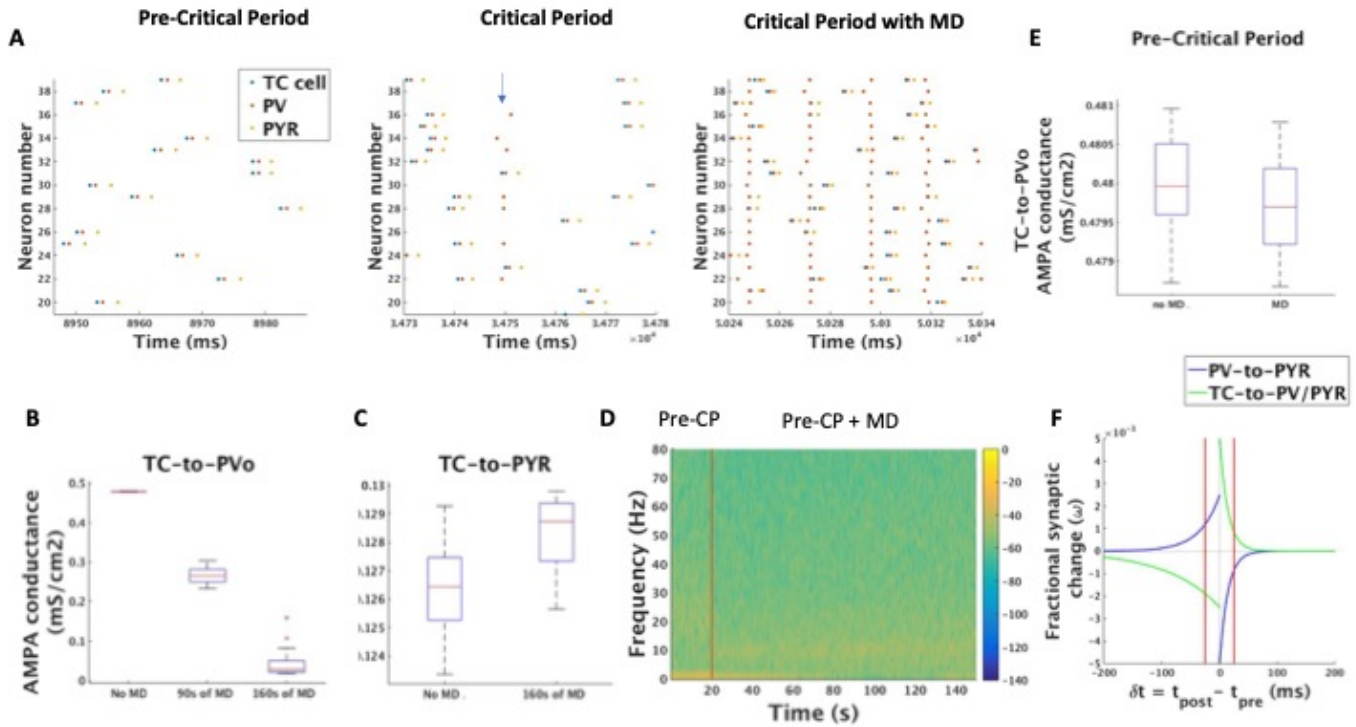
Supp Fig 5: (A) Raster plots of spiking activity of the TC cells, the PVo cells and the PYR cells in the pre-CP, CP and CP MD states. In the pre-CP, the spike timing between the TC cells and the PVo cells is always pre-post for the strong TC-to-PVo synapses. During the CP and during CP MD, spiking between the TC and PVo cells is no longer only pre-post due to synchronous spiking of PVo cells. The blue arrow in the middle raster plot points to a period of time when PVo cells synchronize independent of TC input during the CP. TC to PYR cells remain pre-post under all conditions (pre-CP, CP and CP MD). (B) Boxplots of the AMPA conductance of the strong TC-to-PVo connections during the critical period without MD, as well as during the critical period with MD both at 90s and 160 s of simulation time after the start of MD. (C) Boxplots of the AMPA conductance of the TC-to-PYR connections during the critical period with and without MD after 160 s of simulation time. (D) Spectrogram of the model LFP during the pre-CP before and after MD. Red vertical line marks the start of MD. (E) Boxplots of the TC-to-PVo AMPA conductance before and after MD during the pre-CP. (F) Plasticity rules for model thalamocortical network. STDP from TC cells to either PV or PYR cells follows a Hebbian plasticity rule (green line). STDP from PV cells to PYR cells follows an anti-Hebbian rule that favors the formation of lateral inhibition. Plasticity rules shown out to dt of 200 ms. Red lines mark ± 25 ms to show where plasticity occurs during ING.
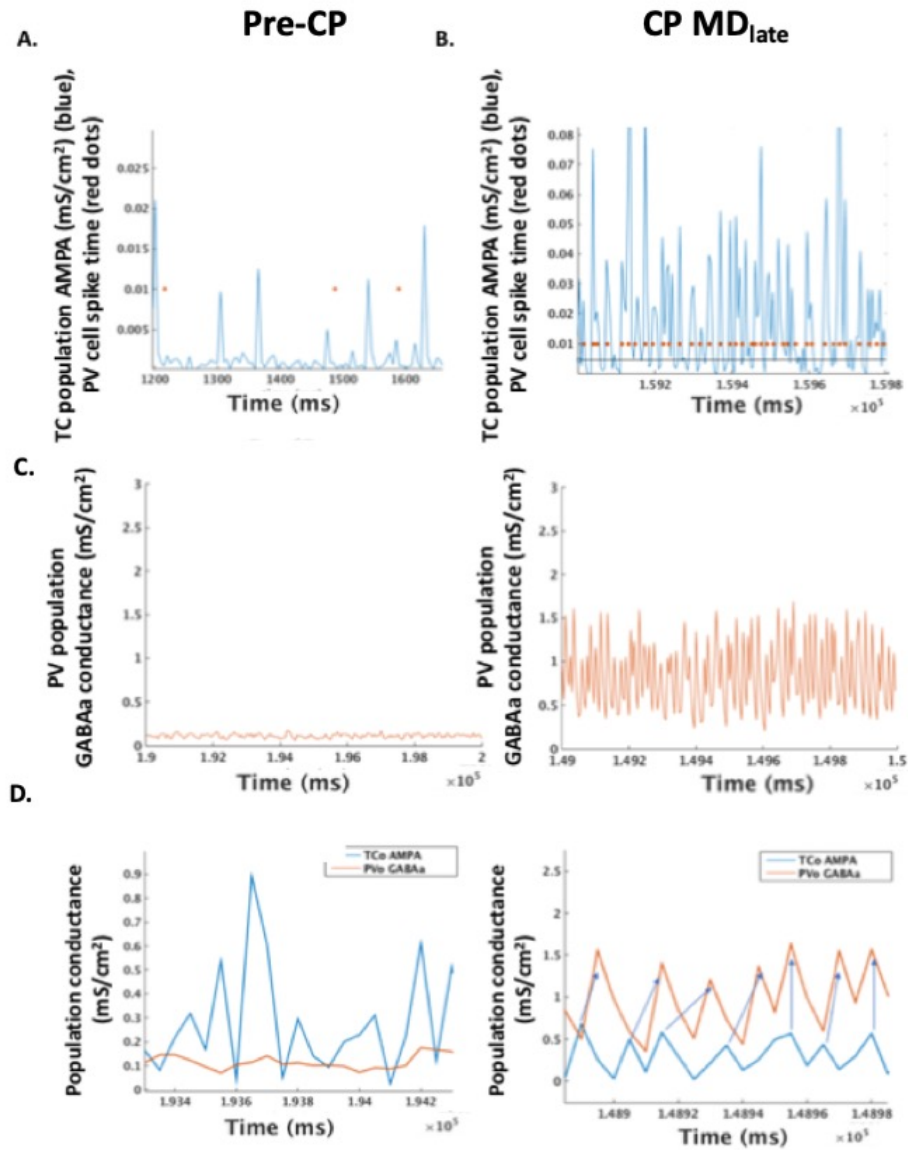
Supp Fig 6: **Network modifications in response to MD during the CP alter network dynamics.** (A) A PV cell does not always spike (red dots) in response to weak population TC AMPA input (blue line) in the pre-CP. (B) The PV cell responds even to weak population TC AMPA input (threshold at 0.005 mS/cm^2, black line) during CP MD$_{late}$ after thalamocortical projections to PV cells become more homogeneous. AMPA conductance represented by blue lines in units of mS/cm^2. Red dots represent times of PV cell spiking. (C) Sum of the GABAa conductance of the population of PVo cells during the pre-CP (left) and during CP MD$_{late}$ after thalamocortical rewiring (right). (D) Sum of the AMPA conductance from the TCo population to the PVo population (blue lines) and sum of the GABAa conductuctance from the PVo population during the pre-CP (left) and after synaptic modifications during CP MD$_{late}$ (right). The arrows show the one-to-one entrainment between the TCo population oscillations and PVo population oscillations during CP MD$_{late}$.
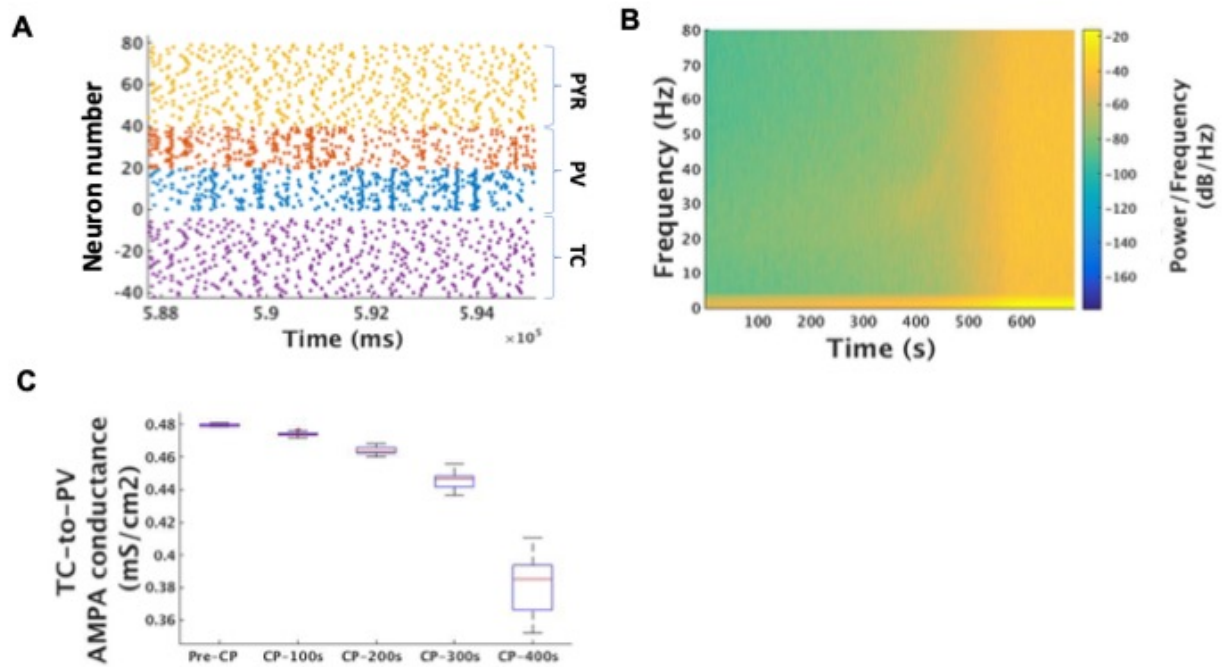
Supp Fig 7: **Critical period dynamics without MD.** (A) Raster plot of all neurons in the thalamocortical network under CP conditions without MD. ING rhythms alternate between the two populations of PV cells (red dots and blue dots). (B) Spectrogram of the model LFP during the CP without MD. Pre-CP simulated from 0 to 20 s, and CP conditions exist after 20 s. (C) Boxplots of the AMPA conductance of the strong TC-to-PV connections during the pre-CP and at simulation time points 100s, 200s, 300s, and 400s after the start of the critical period.
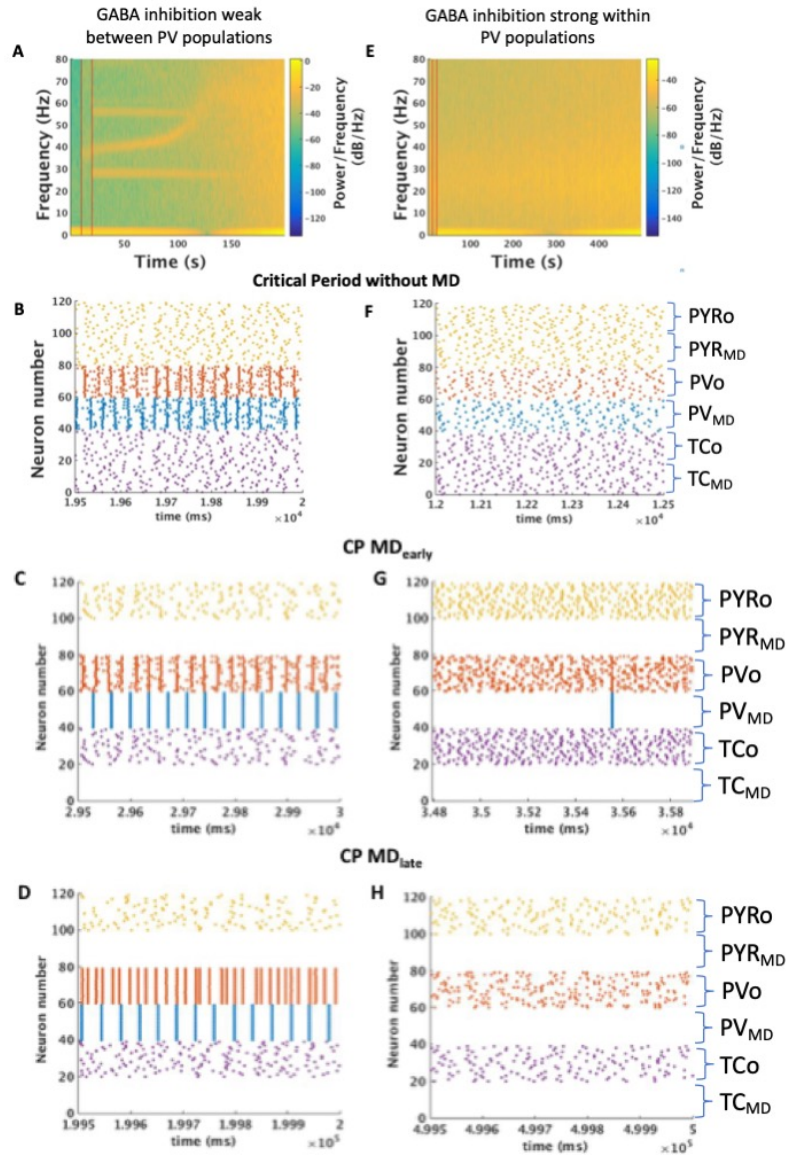
Supp Fig 8: **Network dynamics when GABA conductance used between PV populations equals the GABA conductance used within a PV population.** (A) Spectrogram of model LFP and raster plots of spiking (B) during the CP without MD and (C) during the CP with MD_{early} and (D) during the CP with MD_{late} (last 500 ms of simulation) when gGABA between all PV cells is low (gGABA = 0.03 mS/cm^2 during the CP). (E) Spectrogram of model LFP and raster plots of spiking (F) during the CP without MD (G) during the CP with MD_{early} and (H) during the CP with MD_{late} (last 500 ms of simulation) (H) when gGABA between all PV cells is high (gGABA = 0.25 mS/cm^2 during the CP). Red lines on the spectrogram from left to right mark the transition times between the pre-CP and the CP and between the CP and the CP+MD, respectively.
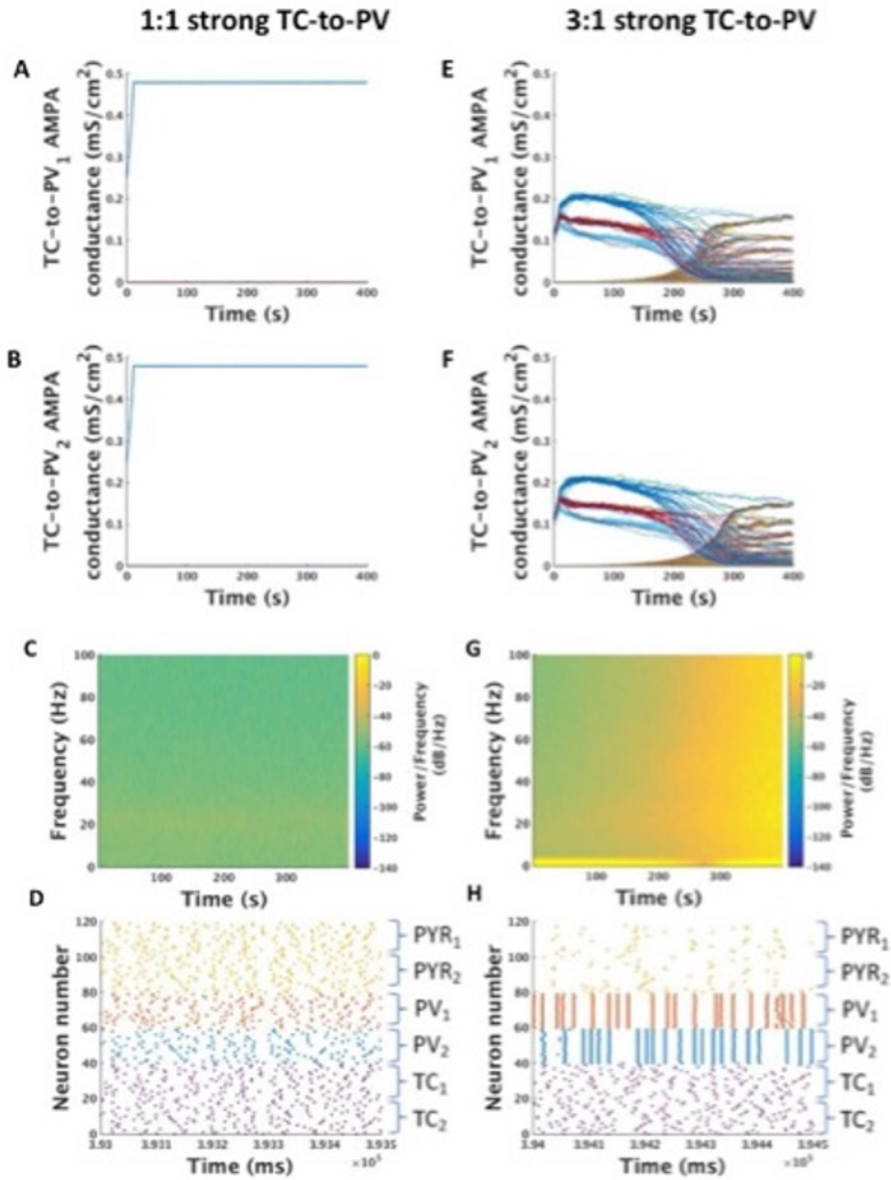
Supp Fig 9: **One-to-one strong TC-to-PV synapses in the pre-CP prevents plasticity.** Evolution of (A) the model TC-to-PV1 synaptic AMPA conductances and (B) the model TC-to-PV2 AMPA conductance throughout the pre-CP when initial TC-to-PV connections are 1:1 strong. PV1 and PV2 are the two populations of PV cells receiving thalamic input originating from the right and left eyes, respectively. (C) Spectrogram of the model LFP during the pre-CP when initial TC-to-PV connections are 1:1 strong. (D) Raster plot of all neurons in the network towards the end of the simulation when initial TC-to-PV connections are 1:1 strong. Evolution of (E) the model TC-to-PV1 synaptic AMPA conductances and (F) the model TC-to-PV2 AMPA conductance throughout the pre-CP when initial TC-to-PV connections are 3:1 strong. (G) Spectrogram of the model LFP during the pre-CP when initial TC-to-PV connections are 3:1 strong. (H) Raster plot of all neurons in the network towards the end of the simulation when initial TC-to-PV connections are 3:1 strong. The subscripts 1 and 2 denote the eye from which the neuron receives its input (in the case of TC cells and PV cells) or its only strong input (in the case of PYR cells).
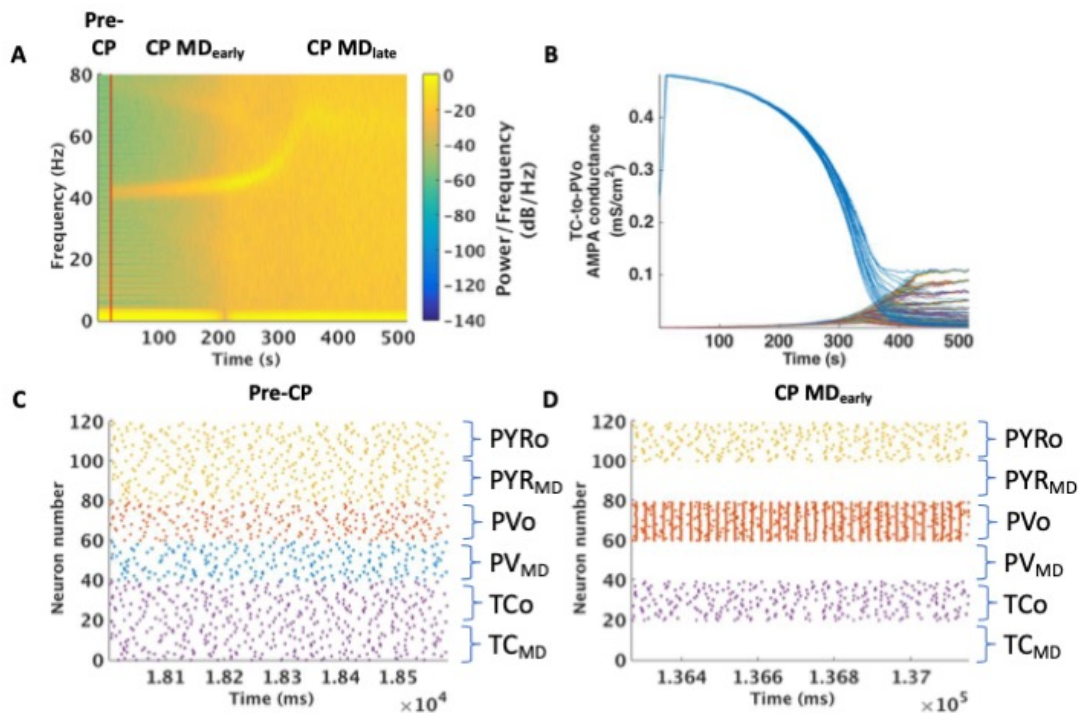
Supp Fig 10: **Network results using an unbiased spike-time counting method.** (A) Spectrogram showing the evolution of gamma in the model LFP during the pre-CP (before red vertical line) and during CP MD_{early} and CP MD_{late}. (B) Evolution of all model TC-to-PVo synaptic AMPA conductances during the same time period as shown in (A). Each line shows the AMPA conductance of one TC-to-PVo synapse over time. (C) Representative raster plots of all neurons in the thalamocortical network during the pre-CP and (D) CP MD_{early} states.
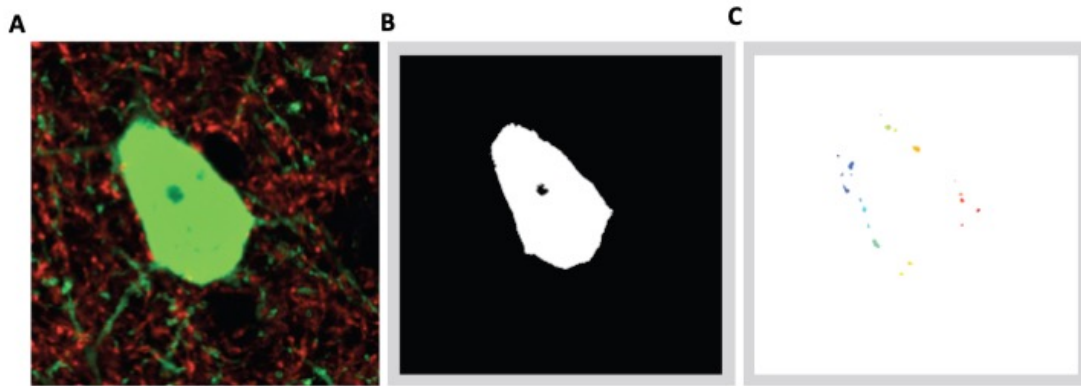
Supp Fig 11: **Automatic Analysis of Synaptic Puncta** (A) Composite image of PV (green) and VGluT2 (red) immunosignal. (B) Automatic thresholding of the green channel to create counting mask. (C) Red channel is segmented based on intensity thresholding (median + 3x S.D.). Counting of puncta restricted within 1.25μm of PV-cell perimeter.

References

[1] Meyer AH, Katona I, Blatow M, Rozov A, Monyer H (2002) In vivo labeling of parvalbumin-positive interneurons and analysis of electrical coupling in identified neurons. J Neurosci 22:7055-7064.

[2] Asada H et al. (1996) Mice lacking the 65 kDa isoform of glutamic acid decarboxylase (GAD65) maintain normal levels of GAD67 and GABA in their brains but are susceptible to seizures. Biochem Biophys Res Commun 229:891-895.

[3] Miwa JM et al. (1999) lynx1, an endogenous toxin-like modulator of nicotinic acetylcholine re-ceptors in the mammalian CNS. Neuron 23:105-114.

[4] Gordon JA, Stryker MP (1996) Experience-dependent plasticity of binocular responses in the primary visual cortex of the mouse. J Neurosci 16:3274-3286.

[5] Takesian AE, Hensch TK. (2013) Balancing plasticity/stability across brain development. Prog Brain Res. 207:3-34.

[6] Hooks BM, Chen C (2006) Distinct roles for spontaneous and visual activity in remodeling of the retinogeniculate synapse. Neuron 52:281-291.

[7] MacLean JN, Watson BO, Aaron GB, Yuste R (2005) Internal dynamics determine the corti-cal response to thalamic stimulation. Neuron 48:811-823.

[8] Barkat TR, Polley DB, Hensch TK (2011) A critical period for auditory TC connectivity. Nat Neurosci 14:1189-1194.

[9] Beierlein M, Gibson JR, Connors BW (2003) Two dynamically distinct inhibitory networks in layer 4 of the neocrtex. J Neurophysiol 90:2987-3000.

[10] Gil Z, Connors BW, Amitai Y (1999) Efficacy of TC and intracortical synaptic connections: quanta, innervation, and reliability. Neuron 23:385-397.

[11] Olufsen MS, Whittington MA, Camperi M, Kopell N (2003) New Roles for the Gamma Rhythm: Population Tuning and Preprocessing for the Beta Rhythm. Journal of Computational Neuroscience 14:33-54.

[12] Mainen ZF, Sejnowski TJ (1996) Influence of dendritic structure on firing pattern in model neocortical neurons. Nature 382:363-366.

[13] Lu, J.T., C.Y. Li, J.P. Zhao, M.M. Poo, and X.H. Zhang, Spike-timing-dependent plasticity of neocortical excitatory synapses on inhibitory interneurons depends on target cell type. J Neurosci, 2007. 27(36): p. 9711-20.

[14] Lee, S., K. Sen, and N. Kopell, Cortical gamma rhythms modulate NMDAR-mediated spike timing dependent plasticity in a biophysical model. PLoS Comput Biol, 2009. 5(12): p. e1000602.

[15] Feldman DE. Timing-based LTP and LTD at vertical inputs to layer II/III pyramidal cells in rat barrel cortex. Neuron. 2000 Jul;27(1):45-56. doi: 10.1016/s0896-6273(00)00008-8. PMID: 10939330.

[16] Debanne D, Gähwiler BH, Thompson SM. Long-term synaptic plasticity between pairs of individual CA3 pyramidal cells in rat hippocampal slice cultures. J Physiol. 1998 Feb 15;507 (Pt 1)(Pt 1):237-47. doi: 10.1111/j.1469-7793.1998.237bu.x. PMID: 9490845; PMCID: PMC2230782.

[17] Reh RK, Dias BG, Nelson CA 3rd, Kaufer D, Werker JF, Kolb B, Levine JD, Hensch TK. Critical period regulation across multiple timescales. Proc Natl Acad Sci U S A. 2020 Sep 22;117(38):23242-23251.

[18] Bi, G. and M. Poo, Synaptic modification by correlated activity: Hebb's postulate revisited. Annu Rev Neurosci, 2001. 24: p. 139-66.

[19] Telenczuk M, Telenczuk B, Destexhe A. Modelling unitary fields and the single-neuron contribution to local field potentials in the hippocampus. J Physiol. 2020 Sep;598(18):3957-3972.

[20] Telenczuk B, Dehghani N, Le Van Quyen M, Cash SS, Halgren E, Hatsopoulos NG, Destexhe A. Local field potentials primarily reflect inhibitory neuron activity in human and monkey cortex. Sci Rep. 2017 Jan 11;7:40211.

[21] Bazelot M, Dinocourt C, Cohen I, Miles R. Unitary inhibitory field potentials in the CA3 region of rat hippocampus. J Physiol. 2010 Jun 15;588(Pt 12):2077-90.

[22] Miller B, Chou L, Finlay BL. The early development of thalamocortical and corticothalamic projections. J Comp Neurol. 1993 Sep 1;335(1):16-41.

[23] Marín O. Thalamocortical topography reloaded: it's not where you go, but how you get there. Neuron. 2003 Jul 31;39(3):388-91.

[24] Agmon A, Yang LT, Jones EG, O'Dowd DK. Topological precision in the thalamic projection to neonatal mouse barrel cortex. J Neurosci. 1995 Jan;15(1 Pt 2):549-61.

[25] Price DJ, et al. (2006) The development of cortical connections. Eur J Neurosci. 23(4):910-20.

[26] Rumpel S, Kattenstroth G, Gottmann K. (2004) Silent synapses in the immature visual cortex: layer-specific developmental regulation. J Neurophysiol. 91(2):1097-101.